Anharmonic motions *versus* dynamic disorder at the Mg ion from the charge densities in pyrope (Mg$_3$Al$_2$Si$_3$O$_{12}$) crystals at 30 K: six of one, half a dozen of the other

Riccardo Destro,[a]* Riccardo Ruffo,[b] Pietro Roversi,[c] Raffaella Soave,[d] Laura Loconte[a] and Leonardo Lo Presti[a,e]

[a]Department of Chemistry, Università degli Studi di Milano, Via Golgi 19, 20133 Milano, Italy, [b]Department of Materials Science, Università degli Studi di Milano-Bicocca, Via Cozzi 55, 20125 Milano, Italy, [c]Oxford Glycobiology Institute, Department of Biochemistry, University of Oxford, Oxford OX1 3QU, England, [d]Istituto di Scienze e Tecnologie Molecolari, Italian CNR, Via Golgi 19, 20133 Milano, Italy, and [e]Centre for Materials Crystallography, Århus University, Langelandsgade 140, 8000 Århus, Denmark. *Correspondence e-mail: riccardo.destro@unimi.it

The possible occurrence of static/dynamic disorder at the Mg site in pyrope (Mg$_3$Al$_2$Si$_3$O$_{12}$), with or without anharmonic contribution to the thermal vibrations even at low temperatures, has been largely debated but conclusions were contrasting. Here a report is given on the experimental charge density distribution, ρ_{EXP}, of synthetic pyrope at $T = 30$ K, built through a Stewart multipolar expansion up to $l = 5$ and based on a very precise and accurate set of in-home measured single-crystal X-ray diffraction amplitudes with a maximum resolution of 0.44 Å. Local and integral topological properties of ρ_{EXP} are in substantial agreement with those of ρ_{THEO}, the corresponding DFT-grade quantum charge density of an ideal pyrope crystal, and those derived from synchrotron investigations of chemical bonding in olivines. Relevant thermal atomic displacements, probably anharmonic in nature, clearly affect the whole structure down to 30 K. No significant ($> 2.5\sigma$) residual Fourier peaks are detectable from the ρ_{EXP} distribution around Mg, after least-squares refinement of a multipole model with anharmonic thermal motion at the Mg site. Experimental findings were confirmed by a full analysis of normal vibration modes of the DFT-optimized structure of the perfect pyrope crystal. Mg undergoes wide displacements from its equilibrium position even at very low temperatures, as it is allocated in a ~ 4.5 Å large dodecahedral cavity and involved in several soft phonon modes. Implications on the interplay among static/dynamic disorder of Mg and lattice vibrational degrees of freedom are discussed.

1. Introduction

Garnets are very common silicates in the Earth's upper mantle. Their general formula, $X_3^{2+}Y_2^{3+}\mathrm{Si}_3\mathrm{O}_{12}$, allows a significant compositional variability, as several combinations of divalent and trivalent cations can be allocated in dodecahedral (X) and octahedral (Y) lattice sites. Structural and elastic properties of garnets determine seismic velocities at different depths (Huang, 2014), lying therefore at the core of any sensible model of the Earth's composition. Moreover, garnet-like structures receive continuous attention, as they find application in cutting-edge industrial applications (Thangadurai *et al.*, 2015), including fabrication of advanced electro-optical devices (Zhong *et al.*, 2015) and high-temperature ion conductors (Pinzaru & Thangadurai, 2014; Geiger, 2013a; Buschmann *et al.*, 2012; Galven *et al.*, 2011). In general, knowledge of the structure and dynamics of complex

30 K · Mg$_3$Al$_2$(SiO$_4$)$_3$ · Harmonic · Anharmonic · Disorder ? · $\Delta\rho = \pm 0.15$ e·Å^{-3} · (100)
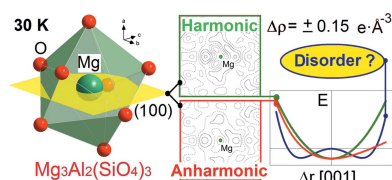
oxides at the atomic scale is mandatory to understand their properties at the macroscopic level. In particular, cation disorder (Schmidt *et al.*, 2015) and anharmonicity effects (Nishimura *et al.*, 2016; Kisi & Yuxiang, 1998) are known to influence lattice stability (Palke *et al.*, 2015) and ion transport properties (Schmidt *et al.*, 2015; Nishimura *et al.*, 2016). Despite ongoing efforts, an unambiguous consent on the actual interplay of cation disorder and anharmonicity does not exist, as they are strongly intertwined and cannot be easily disentangled through routine experimental techniques (Dove, 1997).

In particular, conflicting statements were reported on the mutual occurrence of anharmonicity and cation disorder in the pyrope garnet (Pilati *et al.*, 1996; Armbruster *et al.*, 1992; Sawada, 1993; Pavese *et al.*, 1995; Artioli *et al.*, 1997). This mineral represents a key test case, as it is one of the ideal end-members of a rich wealth of solid solutions of isostructural garnet nesosilicates, including almandine ($Fe_3Al_2Si_3O_{12}$) and grossular ($Ca_3Al_2Si_3O_{12}$). Structural (Andrés *et al.*, 1995; D'Arco *et al.*, 1996), elastic (Erba *et al.*, 2014*a*,*b*; Kawai & Tsuchiya, 2015; Li *et al.*, 2011), electronic (Andrés *et al.*, 1995), spectral (Maschio *et al.*, 2013; Dovesi *et al.*, 2011) and surface (Massaro *et al.*, 2014) properties of pyrope have been the object of several *ab initio* simulations, whereas, on the experimental side, investigations have been carried out to map its thermoelastic properties throughout the p,V and T,V diagrams (Milani *et al.*, 2015), as well as to measure the steady-state plastic properties at high temperature and pressure (Li *et al.*, 2006). Coherent inelastic neutron scattering on a powder sample at $T = 14$ and 30 K (Pavese *et al.*, 1998) aimed to clarify the sources of some thermodynamic anomalies (Haselton & Westrum, 1980), possibly related to static disorder of the Mg atom. Various single-crystal X-ray diffraction (XRD) and neutron diffraction multi-temperature studies (Armbruster *et al.*, 1992; Sawada, 1993; Pavese *et al.*, 1995), as well as lattice dynamic calculations (Pilati *et al.*, 1996; Pavese *et al.*, 1998), were also performed. The diffraction experiments revealed possible anharmonic thermal motion both at room temperature (Sawada, 1993) and at 30 K (Artioli *et al.*, 1997), but the relatively low resolution could not help those authors to decide whether the large anisotropic temperature factor of Mg was indicative of a multi-site distribution of the cation around its crystallographic ordered position. A more recent single-crystal XRD investigation (Nakatsuka *et al.*, 2011) at 20 points in the temperature range 96.7–972.9 K has reopened the debate (Geiger, 2013*b*; Nakatsuka *et al.*, 2013), bringing
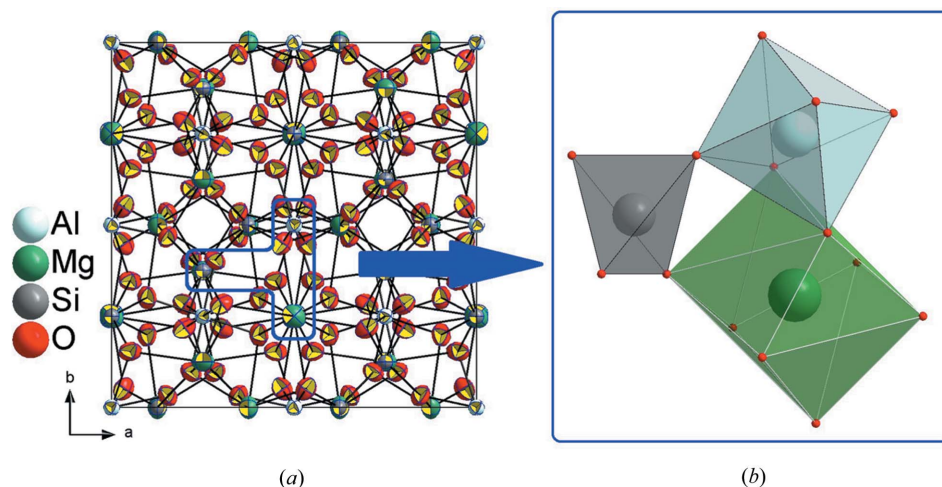

Figure 1
(*a*) Packing scheme of pyrope along the [001] axis, as retrieved from the current single-crystal X-ray analysis at $T = 30$ K. Displacement ellipsoids correspond to a 50% probability level and were all enhanced by a factor 10 to be clearly visible. (*b*) Coordination polyhedra of Al (octahedron), Mg (dodecahedron) and Si (tetrahedron) corresponding to the frame highlighted in (*a*). Realised with *DIAMOND* (Crystal Impact, 2014).

forward X-ray difference Fourier maps as documentation of static disorder.

Here we aim to shed light on this problem by studying the experimental electron density (ED) of synthetic pyrope, $Mg_3Al_2Si_3O_{12}$ (Fig. 1), to an unprecedented level of precision and accuracy at $T = 30.0$ (3) K. The idea is that any statistically significant disorder of Mg^{2+} should be evident in accurate residual density Fourier maps, as both high-order and low-order data carry information on possible deviations from the expected site stoichiometry. DFT-grade periodic calculations, at both the experimental and th optimized lattice geometries, complement experimental outcomes and provide insights on the accuracy of the models proposed to account for the observed ED features at the Mg crystallographic site. We eventually prove that such features might indicate some kind of displacive *dynamic* (not *static*) disorder, as they are strictly related to vibrational degrees of freedom of the lattice and possibly coupled with anharmonic contributions to anisotropic displacement parameters (ADPs).

2. Materials and methods

2.1. Notes on the original data collection

The original pyrope sample was grown by hydrothermal methods (Armbruster *et al.*, 1992) and investigated using XRD at 100 and 293 K. This report is based on XRD data we had collected at $T = 30$ K on the same sample ground to a sphere ($\varnothing \simeq 0.45$ mm) and then used by Pavese *et al.* (1995). However, their data reduction, processing and analysis differ from ours (see §§2.2–2.4 below).

2.2. Data collection

The data collection was performed on a four-circle diffractometer equipped with graphite-monochromated Mo $K\alpha$ radiation (λ = 0.71073 Å) and a Samson cryostat (Samson *et al.*, 1980), where the sample is enclosed in an evacuated, nearly isothermal cavity, ensuring a maximum fluctuation of ±0.3 K. *T* was set to 30 K to make our results as comparable as possible with those from neutron diffraction (*T* = 30 ± 1 K) on a natural sample of pyrope (Artioli *et al.*, 1997).

A total of 7486 diffracted intensities were measured out to $2\theta = 109°$ [$(\sin\theta/\lambda)_{max}$ = 1.14 Å^{-1}] using a scintillation counter point-detector. Consolidated procedures for low-temperature high-quality data collection and reduction were adopted (Destro *et al.*, 2000, 2004, 2005, 2010; Lo Presti *et al.*, 2006; Lo Presti & Destro, 2008). They include: (i) a re-measurement of the strongest reflections at a lower current setting, to minimize problems associated with counter saturation effects, and (ii) measurement of selected profiles at the largest feasible scan width, to evaluate part of the scan-truncation correction (see below). In addition, a second set of data was collected after changing the crystal orientation, to better identify multiple reflections in the subsequent data processing. All other details of the data collection are provided in the supporting information.

2.3. Data reduction

Apart from the absorption correction, discussed in detail in §3.1.1 below, other steps of the data processing were: (i) the identification and rejection of numerous data tainted by the Renninger effect (Renninger, 1937); (ii) the estimation of scan-truncation losses (Destro & Marsh, 1987, 1993; Destro, 1988), which is crucial to determine reliable ADPs; (iii) the corrections for Lorentz and polarization effects; (iv) the merging and weighted averaging of equivalent reflections (R_{merge} = 0.0134), to end up with a set of 788 unique reflections, of which only three had *I* < 0. No thermal diffuse scattering (TDS) correction was deemed necessary, because of the very low temperature at which diffraction data were recorded. Outcomes of statistical tests to assess the quality of the dataset are shown in §3.1. We remark that, at variance with previous crystallographic works on the title compound, we *do not* reject any weak or low-angle positive intensity, such as, for example, the $|F_o| < 6\sigma(F_o)$ and the $\sin\theta/\lambda \leq 0.24$ Å^{-1} classes of reflections (Pavese *et al.*, 1995; Nakatsuka *et al.*, 2011, 2013). The practice of pruning the dataset by excluding data which cannot be reliably reproduced by the structural/ED model, although justified if some measurements are affected by unavoidable biases, necessarily implies a loss of information, which might reflect in rather unpredictable ways into the least-squares outcomes. As a consequence, our description of the thermal motion disagrees, to various extents, with those published so far (see §§3.2 and 3.3). Further details can be found in the supporting information, §§S1–S2.

2.4. Multipole refinements

Least-squares refinements were carried out with the *VALRAY*2000 suite of programs (Stewart *et al.*, 2000), representing the electron density $\rho_{EXP}(\mathbf{r})$ in the framework of the Stewart's pseudoatom formalism (Stewart, 1976). Atomic scattering factors were derived from Stewart's localized atomic orbitals (Stewart, 1980). The interested reader can find full details of the least-squares procedure within the supporting information (§S5). Our final model, labelled hereinafter as ANH, included a multipole expansion of symmetry-allowed poles up to the *l* = 5 level (tricontadipoles) for Al, Mg and Si cations[1] and up to *l* = 4 (hexadecapoles) for the O anion. A single scaling radial parameter κ (KP0 in *VALRAY*2000) was also refined for each atomic species. Oxygen was the only atom allowed to have its crystallographic coordinates relaxed. As for the thermal motion, non-vanishing harmonic ADPs, U^{ij}s, were augmented by Gram–Charlier (GC) coefficients up to the third order (C_{ijk}) for Si and O, and up to the fourth-order (D_{ijkl}) for Mg and Al (see §3.3.2). An attempt was also made to apply fourth-order GC terms to all atoms, but fourth-order tensors of Si and O had negative $^4I_0$ trace invariants (Kuhs, 1992), indicating that their contribution to the atomic p.d.f. is essentially flat. We therefore restricted the GC expansion to the third-order for these atoms. A total of 93 parameters was refined in the last cycles. The refinement process ended with $R(F)$ = 0.0084, $R(F^2)$ = 0.0081, $wR(F^2)$ = 0.0155 and goodness-of-fit = 0.7598. For the 690 data with $F^2 \geq 3\sigma(F^2)$ the agreement index $R(F)$ was 0.0066. The largest features in the residual density ($\Delta\rho$) map were, in e Å^{-3}, +0.12/−0.14 near Si, +0.11/−0.13 near Al, +0.12/−0.12 near Mg, and +0.12/−0.16 near O. The Cruickshank estimate (Cruickshank, 1949) of the e.s.d. in $\Delta\rho$ is 0.058 e Å^{-3}. A full report on the least-squares refinement process is given in §§S4 and S5 in the supporting information.

For comparison purposes, a harmonic ED model (hereinafter HAR) was also developed. It does not include Gram–Charlier cumulants, but it is fully comparable with the ANH one as it relies on the same set of the other 69 parameters. The HAR model refined to $R(F)$ = 0.0091, $R(F^2)$ = 0.0086, $wR(F^2)$ = 0.0169 and goodness-of-fit = 0.8123. More details are available in the supporting information (Model A of Table S4).

Two multipole models which explicitly take into account static disorder of Mg were also refined against F_o. They both include neither Gram–Charlier coefficient nor ED multipoles with $l \geq 1$, and are labelled using the Wyckoff code of the displaced positions of the ion. Thus, model DIS48*f* describes Mg as displaced along the [001] axis from its 24*c* crystallographic site at [0,1/4,1/8] (using 26 parameters), whereas model DIS96*h* includes 28 parameters with the same displacements suggested by Nakatsuka *et al.* (2011) (Tables S10–S11). For comparison purposes a 24*c* monopole only anisotropic refinement, with a total of 27 refined parameters, was also performed (see Tables S12).

---

[1] Tricontadipoles are set to 0 by symmetry for the Al ion, which sits on a 16*a* site with (.$\bar{3}$.) symmetry.

2.5. Theoretical calculations

Fully periodic single-point DFT calculations at the 30 K experimental geometry have been performed with the *CRYSTAL*14 program (Dovesi *et al.*, 2014), employing the same B3LYP functional as Dovesi *et al.* (Erba *et al.*, 2014*a,b*; Maschio *et al.*, 2013) for garnets in conjunction with the pob-TZVP basis set by Peintinger *et al.* (2013). Full details of the calculations are available in §S6 of the supporting information. The crystal structure was also optimized at fixed lattice parameters, exploiting full $Ia\bar{3}d$ symmetry. The coordinates of the cations being fixed, the only change in geometry was a 0.01 Å-large shift of the independent oxygen atom. A full vibrational analysis of the normal modes was also performed on the optimized structure. No negative eigenvalues of the nuclear Hessian matrix at the Γ point were detected, confirming that the lattice does not suffer from structural instabilities. Theoretical ADPs at $T = 30$ K were also estimated from the normal mode analysis through a Debye–Waller (DW) harmonic lattice dynamical approach (Erba *et al.*, 2013). It was thus possible to directly compare quantum dynamic structure factor amplitudes, F_{DSF}, with the experimental ones, F_o (see §3.1.1). B3LYP estimates for ADPs at the Γ point were also confirmed by a PBE calculation with a higher sampling density in the reciprocal space [keyword SHRINK/4 4 in the *CRYSTAL* input stream; see Dovesi *et al.* (2014), Erba *et al.* (2013)]. However, the PBE model implies a worse agreement with the experiment than the B3LYP one, as it would predict a larger shift (0.03 Å) of O from its best multipole-based estimate.

Static structure factors, F_{SSF}, were also obtained at the experimental X-ray geometry. They were employed in the *VALRAY*2000 code (Stewart *et al.*, 2000) to derive a multipole-projected charge density distribution of pyrope, ρ_{MSSF}, fully comparable with the experimental density. Full details on this multipole model can be found in §S6. Final agreement factors were as low as $R(F) = 0.0026$, $R(F^2) = 0.0023$, and $wR(F^2) = 0.0043$, with a goodness-of-fit of 0.1341. The residual density maps around the three cations can be considered as completely featureless at the cation positions, showing no residuals greater than 0.035 e Å^{-3} in absolute value. Somewhat larger residues (+0.051/–0.053 e Å^{-3}) were observed at

0.784 and 0.507 Å, respectively, from the O atom. A list of the final values for all the refined parameters is reported in Table S6.

3. Results and discussion

3.1. Quality assessment of the procedure

3.1.1. Dataset. Due to the large dimensions of the specimen ($\varnothing \simeq 450$ μm, see §2.1 above), together with the presence of strong absorbers ($\mu = 1.218$ mm^{-1} for Mo $K\alpha$ radiation), great care was taken to deal with absorption and extinction effects. Actually, even a slight deviation of the crystal from a perfectly spherical shape might produce large relative errors on the corresponding corrections. ψ-scans collected at 17.6 (3) K showed that no significant shape-dependent anisotropy affects the measured intensities, apart from some sharp spikes due to Renninger reflections (Renninger, 1937).

Individual measures affected by multiple reflections were accurately removed from the current dataset before merging (see §2.3). As a representative example, the azimuthal scan plot of reflection (022) at 17.6 (3) K is reported in Fig. 2. After removal of patent biases due to multiple reflections, no significant ψ-dependent oscillations are appreciable from the average intensity, $\langle I \rangle = 1.40$ (2) $\times 10^5$ in arbitrary units (Fig. 2*b*) Thus, a perfect spherical shape was assumed to be reasonably accurate. A ($\sin \theta/\lambda$)-dependent empirical correction for absorption was carried out according to *International Tables for Crystallography* (1959, Vol. II, pp. 302–305). The final set of data showed a very good internal agreement among equivalent reflections ($R_{int} = 0.0134$).

Secondary extinction was also explicitly taken into account throughout the *VALRAY* refinement procedure. An isotropic model for a Type I crystal with a Lorentzian distribution of mosaicity was applied to correct observed structure-factor amplitudes of low-angle intense reflections. The extinction parameter refined to 0.245 (6), that is 2450 rad^{-1}, which corresponds to an average mosaic spread of 27″ of arc. Most extinction-affected reflections are the allowed (h00) at low Bragg angle, *i.e.* in particular (400) and (800). The maximum extinction was shown by reflection (400) with a reduction of intensity of 14.6% [*VALRAY* $Y_{EXT} = 0.854$]. Only three other reflections showed a reduction greater than 5%, whereea 12 more had Y_{EXT} between 0.95 and 0.98. The grounding of the crystal (Pavese *et al.*, 1995) and the previous data collection at $T = 100$ K by Armbruster *et al.* (1992) might have increased the mosaicity and hence reduced the extinction.

Once the extinction coefficient is taken into account, the agreement between measured structure-factor amplitudes and DFT-predicted dynamic ones, F_{DSF} (Erba *et al.*, 2013; §2.5) is excellent (Fig. 3), with a maximum overall deviation from
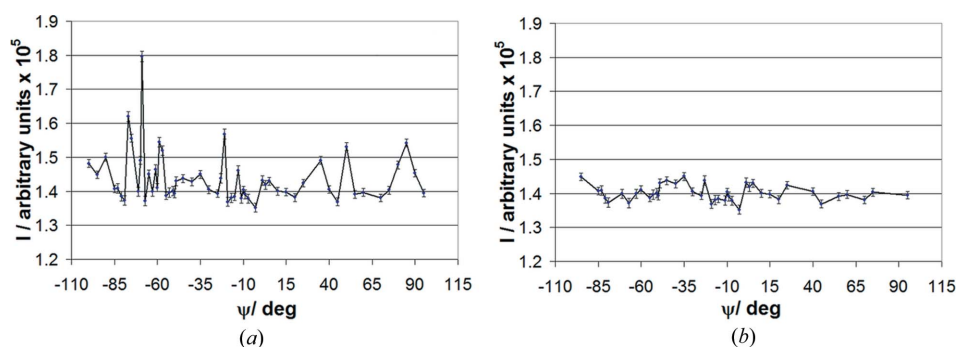

Figure 2
(*a*) Azimuthal ψ-scan of the (022) reflection of pyrope at $T = 17.6$ (3) K. Error bars correspond to two estimated standard deviations. Spikes are due to the Renninger effect. (*b*) Same as (*a*), after removal of contaminant multiple reflections. The broken lines serve as a guide to the eye.

Table 1
Relevant interionic distances (Å) and angles (°) in pyrope at $T = 30$ K.

Estimated standard deviations in parentheses. The numbers in square brackets indicate the frequency of occurrence.

SiO$_4$ tetrahedron	Si—O	1.6354 (4) [4]		
	O—O	2.4998 (5) [2]	2.7519 (5) [4]	
	O—Si—O	99.69 (2) [2]	114.57 (2) [4]	
Al O$_6$ octahedron	Al—O	1.8848 (3) [6]		
	O—O	2.6118 (5) [6]	2.7182 (5) [6]	
	O—Al—O	87.71 (2) [6]	92.29 (2) [6]	180.0 (1) [3]
MgO$_8$ dodecahedron	Mg—O	2.1960 (4) [4]	2.3326 (4) [4]	
	O—O	2.4998 (5) [2]	2.6118 (5) [4]	2.6980 (5) [4]
		2.7690 (5) [2]	3.3034 (5) [4]	3.6869 (5) [2]
	O—Mg—O	69.70 (1) [2]	70.37 (1) [4]	72.82 (1) [2]
		73.07 (1) [4]	93.63 (1) [4]	109.50 (1) [2]
		114.17 (1) [2]	124.32 (1) [4]	160.50 (1) [2]
		164.07 (1) [2]		
Cation–cation separations†	Al—Mg	3.1977 (1) [6]		
	Mg—Si	2.8601 (1) [2]	3.5029 (1) [4]	
	Al—Si	3.1977 (1) [6]		
Cation–oxygen–cation angles‡	Si—O—Al	130.44 (2)		
	Mg—O—Mg	101.30 (1)		
	Mg—O—Si	95.46 (2)	123.00 (2)	
	Mg—O—Al	98.05 (2)	102.92 (2)	

† All distances < 3.6 Å are reported.   ‡ Only cations directly bonded to a given oxygen atom are considered.

the ideal $y = x$ straight line of roughly 1.2 (1)%. Small deviations from linearity affecting reflections of intermediate intensity ($\simeq 20 \times 10^3$) are attributable to the slight difference in the estimated position of O atoms in the two models (see §2.5) and to the inability of the quantum calculation to reproduce effects due to deviations from the ideal perfect lattice model, such as disorder and anharmonicity (see §3.3.2). However, the strong linear correlation supports the high quality of the present dataset.
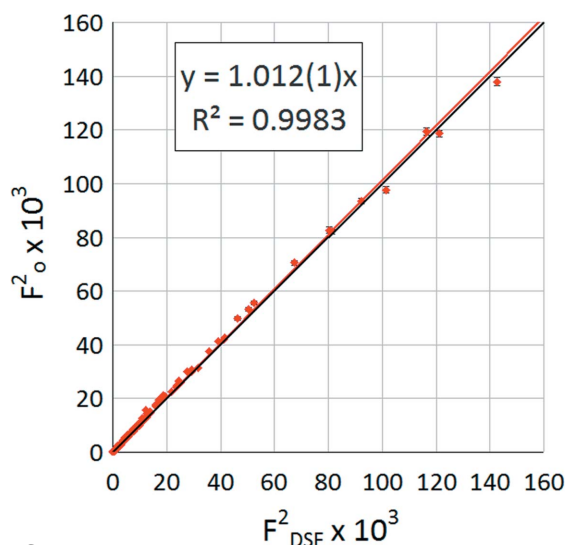

Figure 3
Comparison of symmetry-independent squared amplitudes of dynamic structure factors, as predicted through the normal modes analysis of the DFT B3LYP-optimized geometry of pyrope, F^2_{DSF}, with the corresponding set of 788 measured ones, F^2_o. The red line is the linear least-squares fitting to which statistical parameters in the box refer, while the black line indicates the quadrant bisector, $y = x$, which would occur in the case of an ideally perfect agreement. Vertical bars correspond to the ±1 experimental estimated standard deviation.

3.1.2. Multipole model. The data-to-parameter ratio in the final ANH model (see §2.4) is 8.4, which is relatively low when compared with modern crystallographic studies with synchrotron X-rays (Christensen *et al.*, 2010; Kastbjerg *et al.*, 2013; Jørgensen *et al.*, 2014; Mondal *et al.*, 2016). We therefore applied the free-R test (Brünger, 1992) to check the reliability of the least-squares model against overfitting. More in detail, we performed from scratch a least-squares refinement on 710 unique reflections ('training set'), after having randomly excluded 78 data (10%) from the original set of 788 observations to form a 'cross-validation set'. We then computed the R_{free} agreement factor on the cross-validation set alone, using the same ED and thermal motion parameters developed on the training set, and corresponding to those of the ANH model. The whole procedure was repeated five times, each time changing the random set of reflections in the cross-validation group. The free $R(F)$ factor varies between 0.0091 and 0.0139, providing an average estimate of 0.0118 (8), which is just 0.003 higher than the average $R(F)$ factor for the training set [0.0084 (1)]. This rules out significant overfitting issues with a reasonable confidence. Furthermore, the relative average F_o/F_c agreement as a function of $\sin \theta/\lambda$ for the ANH model is very good (Fig. 4), with largest deviations not exceeding 1.5%.

3.2. Geometry and Debye–Waller factors

Pyrope, Mg$_3$Al$_2$(SiO$_4$)$_3$, formula weight 403.12 g mol^{-1}, crystallizes in the cubic system [$a = 11.4405$ (3) Å at 30 K and $a = 11.4622$ (7) Å at 292 K, calculated density 3.576 g cm^{-3} at 30 K], space group $Ia\bar{3}d$ (No. 230), with $Z = 8$ and $F(000) = 1600$ e. Our experimental estimate of the unit cell edge at 30 K is virtually identical to that measured by Bosenick & Geiger (1997) in a powder X-ray diffraction study of synthetic pyrope at $T = 20$ K. Our value is also the same, within experimental
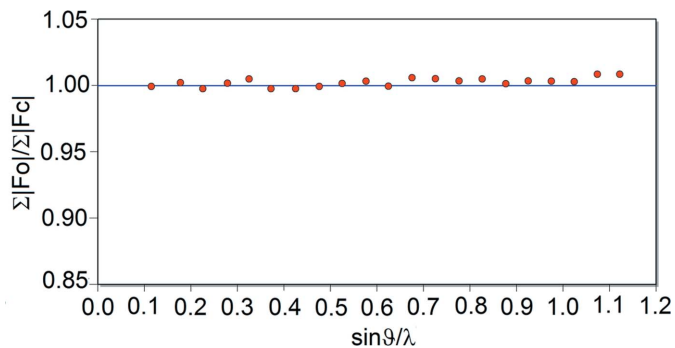

Figure 4
Ratio between the sums of observed and calculated structure-factor amplitudes as a function of $\sin \theta/\lambda$ (Å^{-1}). The graph was computed with the *DRKplot* (Stash, 2007).

Table 2
Comparison of atomic fractional coordinates and Debye–Waller parameters ($Å^2$, multiplied by 10^2), as estimated from this work and other studies.

For each atom, the reference coordinates are given, together with the corresponding site point symmetry and Wyckoff labels.

	XRD ANH, 30 K†	XRD HAR, 30 K‡	LCGTF, B3LYP [PBE]§	XRD, 30 K¶	Neutrons, 30 (1) K††	XRD, 96.7 K‡‡
Si [0, 1/4, 3/8], .4., 24d						
U^{11}	0.180 (2)	0.173 (2)	0.14 [0.15]	0.172 (1)	0.28 (2)	0.270 (1)
U^{22}	0.180 (2)	0.173 (2)	0.14 [0.15]	0.172 (1)	0.28 (2)	0.270 (1)
U^{33}	0.153 (2)	0.147 (2)	0.12 [0.12]	0.150 (2)	0.30 (3)	0.231 (3)
Al [0, 0, 0], $\bar{3}$., 16a						
U^{ii}	0.217 (4)	0.194 (2)	0.16 [0.16]	0.188 (1)	0.28 (2)	0.292 (1)
U^{ij}	0.001 (3)	0.0000 (9)	0.0 [0.0]	−0.002 (1)	0.002 (3)	0.003 (2)
Mg [0, 1/4, 1/8], 2.22, 24c						
U^{11}	0.485 (7)	0.434 (3)	0.38 [0.34]	0.418 (2)	0.46 (2)	0.36 (5)§§
U^{22}	0.485 (7)	0.434 (3)	0.38 [0.34]	0.418 (2)	0.46 (2)	
U^{33}	0.298 (8)	0.269 (3)	0.22 [0.22]	0.261 (3)	0.30 (3)	
U^{12}	0.096 (5)	0.077 (2)	0.07 [0.05]	0.075 (3)	0.04 (2)	
O [x, y, z], 1, 96h						
x	0.03282 (3)	0.03291 (1)	0.03204 [0.03181]	0.032907 (8)	0.03331 (9)	−0.03290 (4)
y	0.05077 (3)	0.05069 (1)	0.05123 [0.05285]	0.050688 (8)	0.05076 (9)	0.05061 (4)
z	0.65326 (3)	0.65334 (1)	0.65305 [0.65293]	0.653311 (8)	0.65310 (10)	0.65333 (4)
U^{11}	0.321 (4)	0.316 (4)	0.26 [0.26]	0.290 (3)	0.39 (2)	0.366 (3)
U^{22}	0.375 (4)	0.370 (4)	0.31 [0.30]	0.354 (2)	0.39 (2)	0.432 (3)
U^{33}	0.261 (4)	0.254 (4)	0.20 [0.21]	0.238 (2)	0.35 (2)	0.352 (3)
U^{12}	0.040 (2)	0.042 (2)	0.03 [0.03]	0.036 (2)	0.02 (1)	−0.048 (2)
U^{13}	−0.057 (2)	−0.057 (2)	−0.05 [−0.05]	−0.064 (2)	−0.01 (1)	0.070 (2)
U^{23}	0.009 (2)	0.007 (2)	0.0 [0.0]	0.005 (2)	0.00 (1)	0.019 (2)

† This work. Estimated from the ANH multipole refinement against F_os. ‡ This work. Estimated from the HAR multipole refinement against F_os (as ANH, with no cumulants). § This work. Linear combination of Gaussian-type function (LCGTF) results, with B3LYP vibration modes at the Γ point. Analogue results for non-hybrid PBE vibration modes at eight points in the first Brillouin zone are reported in square brackets. ¶ Pavese *et al.* (1995), XRD estimates from the same single-crystal employed here. Fourth-order Gram–Charlier coefficients were explicitly refined. †† Artioli *et al.* (1997), neutron diffraction estimates from a *natural* pyrope single crystal. Gram–Charlier coefficients were explicitly refined up to the fourth order. ‡‡ Nakatsuka *et al.* (2011), XRD estimates from another synthetic pyrope single crystal. §§ In their final model, including static disorder on the Mg site, Nakatsuka *et al.* (2011) refined just an isotropic displacement parameter, U_{iso}. Also an $U_{eq} = 0.539$ (1) $\times 10^{-2}$ $Å^2$ estimate was given by these authors in their Table 2 from a harmonic refinement.

error, as that determined by neutron diffraction at the same temperature of 30 K, on a natural sample with 92% Mg, 5% Fe, and 3% Ca at the Mg site (Artioli *et al.*, 1997). There are only four atoms in the asymmetric unit, namely one atom per atomic species of the formula unit. The Al, Mg and Si atoms lie, respectively, in the 16a, 24c, and 24d positions of $Ia\bar{3}d$, of point symmetries $\bar{3}$, 2.22 and $\bar{4}$, respectively. In our treatment, the fractional coordinates of these atoms were assigned as 0, 0, 0 (Al); 0, 1/4, 1/8 (Mg); and 0, 1/4, 3/8 (Si).

The oxygen atom, in position 96h, has the unrestricted coordinates x, y, z to be determined and refined. Table 1 shows the relevant coordination geometries of Si, Al and Mg as determined by the present XRD study at 30 K, whereas Table 2 compares coordinates and harmonic thermal parameters from the present study with those reported in past X-ray and neutron studies.

Our best estimate for the oxygen position is identical to that of Pavese *et al.* (1995) within three estimated standard deviations of the present study. Both estimates are comparable with the neutron diffraction one from Artioli *et al.* (1997) (Table 2), with a maximum deviation of 4–5 neutron e.s.d.'s for the x coordinate of the anion. As expected, such discrepancies are far more significant if weighted by the lower X-ray e.s.d.'s. However, the maximum X-ray/neutron displacement of oxygen is as low as 0.006 Å, even lower than that produced by the lattice relaxation at the DFT level (see Table 2 and §2.5 above). The origin of such differences might be thus traced back to the different nature of the two samples (synthetic *versus* natural), and in particular to the significant substitution of larger cations at the Mg site in the neutron case.

The Debye–Waller parameters estimated in this work, with lattice anharmonicity included (see §3.3.2), are qualitatively comparable to the neutron diffraction results, though somewhat smaller (Table 2). Interestingly, the largest differences concern Si and O atoms, whose cumulant expansion of the atomic probability density functions (p.d.f.'s) up to the fourth order in the neutron case, was here truncated at the third order (§3.3.2). This is a general result: adding higher-order cumulants implies that higher least-squares estimates of the Debye–Waller parameters are obtained as well (compare the first two columns in Table 2). Similar, and even larger, increases of thermal parameters and their e.s.d.'s in the fourth-cumulant refinement had been reported by Thornley and coworkers in a neutron diffraction of the thermal motion at 77 K in cubic nickel iodine boracite, where correlation coefficients $\simeq 0.9$ were observed between U^{ii} and D_{iiii}. Accordingly, the U^{ij} by Pavese *et al.* (1995) show a better agreement with our fully harmonic DFT predictions for atomic ADPs, but at the same time their estimates are significantly lower than the neutron ones at the same temperature (Table 2). Actually, these authors included in their final least-squares model third-order cumulants only on Mg, which turned out to be very small. Thus, their description of the atomic p.d.f.'s is necessarily closer to the fully harmonic one.

3.3. The charge density model

3.3.1. Residual density features. Fig. 5 shows the experimental residual Fourier features, $\Delta\rho_{EXP}$, in the (100) plane around each metal ion in pyrope for (*a*) the independent atom model (IAM), as a suitable spherical-atom reference; (*b*) the HAR multipole model, without higher-order cumulants (§2.4); (*c*) the fully anharmonic ANH one (§2.4). As expected, the

IAM features are dominated by ED holes due to the higher oxidation states of cations with respect to their neutral counterparts, but some structured residual features in the valence shell, due to anisotropic interactions in their first coordination shell, are already evident. The inclusion of multipole and Gram–Charlier parameters in the least-squares procedure significantly reduces the intensity of residual features, including those along chemical bonds. Actually, no residues larger than $+0.12/-0.16$ e Å^{-3} are appreciable in the ANH model. The most relevant structured feature consists of a pair of ED maxima close to Mg (site 24c), $+0.12$ e Å^{-3} in magnitude and ~ 0.58 Å apart from the ion, along the [001] direction (Fig. 5). However, they are both associated with very close negative peaks, -0.12 e Å^{-3} deep, along the same direction. It is hard to attribute some kind of structural effect to such positive features of $\Delta\rho$, as they are not neatly distin-guishable from Fourier fluctuations in the close neighbour-hood of the Mg^{2+} ion. These data seriously pose into question the occurrence of *static* disorder related to Mg^{2+} displacement.

We believe that a possible explanation for such small resi-dual Fourier features might be related to the treatment of the thermal motion. A resolution of $\sin\theta/\lambda > 1.8$ Å^{-1}, much higher than that available to in-home facilities, would add a full description of the anharmonic contributions to the Mg p.d.f. (see §3.3.2). From a purely statistical viewpoint, it is worth noting that explicit inclusion of anharmonicity significantly improves the quality of the fitting. Actually, the Hamilton *F*-test (Hamilton, 1965) was satisfied to a level of significance α of 0.005 when the HAR model was compared with the ANH one under the null hypothesis of a purely harmonic motion. Both recently and in the past, analogue statistical tools were employed to assess the relevance of anharmonic effects in crystals (Christensen *et al.*, 2013; Sørensen *et al.*, 2003; Thornley *et al.*, 1976).

3.3.2. Anharmonicity or dynamic disorder: six of one, half a dozen of the other.

What is at stake here is the interpretation of the structured residual charge density features described above (§3.3.1). The latter have also been detected in previous studies and attributed to some kind of static disorder (Nakatsuka *et al.*, 2011, 2013). Gram–Charlier expansion of atomic probability density func-tions might provide an alternative explanation for structured Fourier peaks, as it is well known that static disorder and anharmonicity produce very similar effects in $\Delta\rho$ maps (Scheins *et al.*, 2010), even though it has been recently reported (Herbst-Irmer *et al.*, 2013) that a 'shashlik-like' alternation of positive and negative ED residuals might be specifically associated with anharmonic behaviour. Infor-mation on anharmonicity is mainly brought by high-order reflections, as shown by Kuhs (1992) by differentiating the expression of the generalized Debye–Waller factor to find the Q limit where the contributions of higher anharmonic terms are maxima. However, the Kuhs' formula should be consid-ered, as said by Kuhs himself (Kuhs, 1992, p. 93) as '*a rule of thumb*' to decide to what extent the data collection should be carried out '*for refining successfully terms*
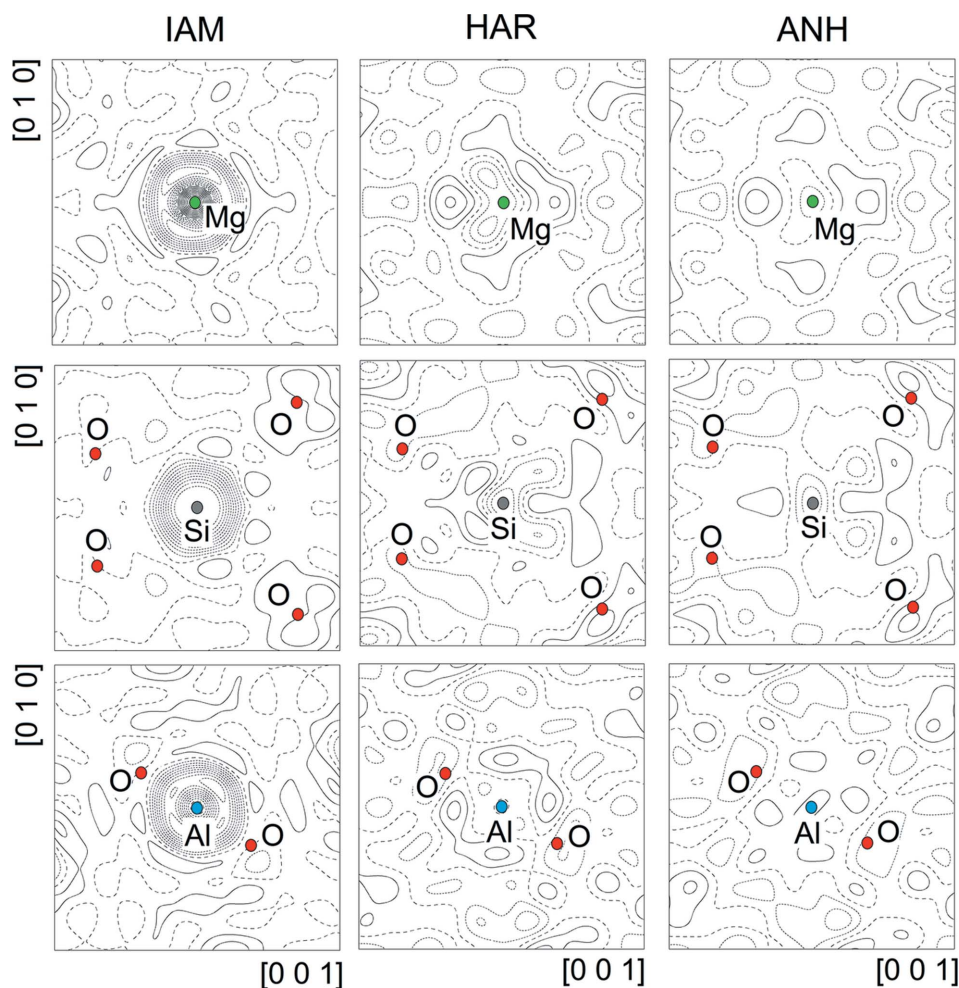

Figure 5
Residual Fourier maps, $\Delta\rho_{\text{EXP}}$ against measured structure-factor amplitudes compared with structure factors predicted from (i) the independent atom model, with spherical and neutral atoms (left column), (ii) the fully harmonic HAR model (central column) and (iii) the final multipole model, with anharmonic contributions explicitly considered (right column). All the maps are 3×3 Å wide within the (100) plane, with Mg (first row), Si (second row) or Al (third row) at the centre of each plot. Contour levels are drawn at steps of either 0.2 e Å^{-3} (IAM maps) or 0.05 e Å^{-3} (HAR and ANH maps), with full (dotted) lines representing positive (negative) values. The dashed curve corresponds to the $\Delta\rho = 0$ level. O atoms on the left side of the Si maps are out of plane by ± 1.1 Å, those on the right side by ± 0.6 Å. In Al maps, the O atoms are out of plane by ± 1.8 Å.

of order n' of the Gram–Charlier expansion. Indeed, anharmonic behaviour affects low-order reflections as well, though to a minor extent, and, as a consequence, also the local features of the deformation charge density (Kuhs, 1988). Nevertheless, insufficient data resolution makes it much difficult – and often impossible – to extract such information from the observed structure-factor amplitudes. However, in this respect, the data quality is also an important discriminator.

As for the present case, the available resolution of our dataset is too low to fulfil Kuhs' condition. This reflects in a minority of high (> 0.707) least-squares correlation coefficients among positional and thermal parameters of the anion (see below). Moreover, the oscillating Fourier features detected close to the Mg 24*c* site (§3.3.1) are also likely related to resolution issues. However, we are confident that the quality of our dataset is high enough to detect, if present, any significant effects affecting low-order diffraction intensities. Multipole modelling was complemented with independent infomation coming from periodic quantm calculations (see below and §2.5). We also compared alternative multipole models, where the disorder was explicitly taken into account (see below and §2.4), to those based on a fully ordered model of the crystal. This strategy is motivated by the fact that any deviation from the expected site stoichiometry has an impact on the real-space description of atomic scattering centres, and specifically on monopole populations, thermal motion parameters and site occupation factors. Thus, if the hypothesis of static disorder at the Mg site was correct, the quality of the fitting should have been improved against any comparable model of the ordered crystal.

There is also another consideration to be pointed out. Disorder – both static and dynamic – invariably implies that a double- (or multiple?)-well potential is present at the Mg 24*c* site (Fig. 6).
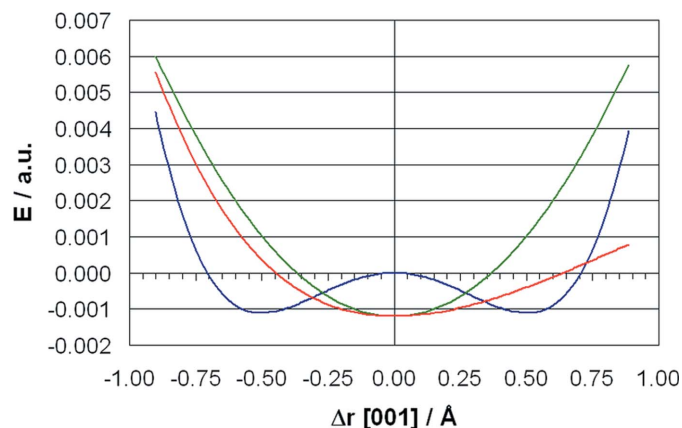

Figure 6
Example to illustrate the difference among a purely harmonic (parabolic green curve), an anharmonic (red curve) and a double-well (blue curve) potential. Energy is given in atomic units as a function of the displacement (in Å) of the Mg atom from its crystallographic position along the [001] direction. Arbitrary functional forms were assumed, namely $E = E_0\Delta r^2 + C$ (harmonic), a Morse form $E = E_0[1 - \exp(-\alpha\Delta r)]^2 + C$ (anharmonic) and a quartic function $E = E_0(C\Delta r^4 - \Delta r^2)$ (double-well).

Therefore, disorder is necessarily entangled with some kind of anisotropy in the crystal field, which might be produced, for example, by a symmetry breaking of the perfect Mg dodecahedral cage. Whereas this symmetry breaking should be small in the case of dynamic disorder, the existence of two or more well defined minima, separated by intersite barriers high enough to hamper Mg exchange among populated off-lattice sites even at $T \gg 30$ K (Fig. 6; Nakatsuka *et al.*, 2011), would imply a much larger distortion. We thus expect that *static* disorder is accompanied by some other kind of defect-induced lattice distortions (defect clustering? oxygen non-stoichiometry?), and indeed Nakatsuka *et al.* conclude that other ions rather than Mg could be statically disordered in pyrope. However, we do not see any evidence for that, neither on the Mg atom nor on any of the other atoms in the asymmetric unit. For example, any significant displacement of oxygen from its crystallographic general position (96*h*) should have produced a constellation of structured residual peaks in the F_o–F_c maps, in conjunction with a negative residual at the nucleus, but this is not the case (Fig. 5). The only relevant structured Fourier feature we detected is an alternation of positive and negative peaks across the Mg site (Fig. 5). Such peaks, which are invariably smaller than 0.10–0.15 e Å^{-3}, lie along one of the [001], [010] and [100] directions, depending on the specific site considered. Positive features lie ~ 0.58 Å apart from the ion in a 48*f* site and could perhaps be associated with some kind of static positional disorder. However, any attempt to explicitly include 48*f*-disordered Mg in the multipole model, refining its fractional coordinates and monopole electronic parameters (model DIS48*f*, see §2.4 and Table S11), invariably implies that the ion is brought back to its original, undisplaced 24*c* position within a few (< 2) thousandths of Å. We would have expected that the information on Mg static site disorder was present in accurate X-ray structure-factor amplitudes measured up to a maximum resolution of sin $\theta/\lambda = 1.14$ Å^{-1} at $T = 30$ K. It could be objected that the displacement of Mg from its crystallographic 24*c* position is very small. Nakatsuka *et al.* (2011), for example, found a maximum Mg displacement of 0.07 Å to a general position 96*h*, even though they also note that many higher-rank anharmonic coefficients deviate significantly from zero at 96.7 K. These authors indeed conclude that '*it is certain that the probability density functions ... of all atoms are significantly deformed from ellipsoidal distributions even at a low temperature*', but attribute such deformation to *static* disorder rather than to anharmonic contribution to the thermal motion. As a possible check of the reliability and robustness of their displacive disorder model on Mg, we applied the latter to our data through the DIS96*h* model (see §2.4 and Table S10). We accordingly estimated a slightly lower value (0.06 Å) for the Mg displacement. However, the refined position lies within the envelope of the harmonic thermal ellipsoid of Mg at the 50% probability level. Moreover, the agreement of the 96*h*-disordered model (isotropic Mg) with our complete set of 785 observed structure-factor amplitudes[$wR(F^2) = 0.0283$] is considerably worse than the comparable monopole-only refinement (anisotropic Mg, Table S12) corresponding to the 24*c*-ordered structure [$wR(F^2) = $

Table 3
Comparison of adimensional third- and fourth-order Gram–Charlier coefficients (multiplied by 10^4), as estimated from this work and other studies.

For each atom, the reference coordinates are given, together with the corresponding site point symmetry and Wyckoff labels. Symmetry constraints are shown in the first column.

	XRD ANH, 30 K†	Neutrons, 30 (1) K‡§	XRD, 96.7 K¶	XRD, RT††
Si [0, 1/4, 3/8], .4., 24d				
C112 = (−C223)	0.013 (2)	< 2σ	//	0.001 (2)
C123	−0.019 (4)	//	//	−0.005 (5)
Al [0, 0, 0], $\bar{3}$., 16a				
D1111 (= D2222 = D3333)	0.0007 (1)	< 2σ	∼ −0.00006 (1)	0.00002 (6)
D1112 (= D1333 = D2223)	0.0003 (2)	< 2σ	//	−0.0001 (1)
D1122 (= D1133 = D2233)	0.0007 (2)	< 2σ	∼ −0.00006 (2)	0.0002 (2)
D1113 (= D1222 = D2333)	0.0001 (2)	//	//	0.0002 (1)
D1123 (= D1223 = D1233)	0.0000 (3)	< 2σ	//	0.0002 (2)
Mg [0, 1/4, 1/8], 2.22, 24c				
C113 (= −C223)	−0.014 (3)	−0.2 (2)	Not included	−0.0002 (1)
D1111 (= D2222)	0.0013 (2)	//		−0.0003 (2)
D1112 (= D1222)	0.0015 (4)	< 2σ		0.0000 (4)
D1122	0.0040 (6)	< 2σ		−0.0003 (2)
D1133 (= D2233)	0.0014 (4)	−0.3 (2)		0.0002 (5)
D1233	0.0009 (7)	< 2σ		−0.0001 (1)
D3333	0.0008 (3)	//		−0.0002 (1)
O [x, y, z], 1, 96h				
C111	−0.013 (4)	0.6(4)	//	0.001 (2)
C112	0.013 (5)	< 2σ	//	0.004 (3)
C122	−0.002 (5)	< 2σ	//	−0.003 (3)
C113	−0.016 (5)	< 2σ	//	−0.007 (3)
C123	0.001 (6)	< 2σ	0.004 (< 1)	−0.002 (5)
C133	−0.014 (5)	< 2σ	//	0.002 (3)
C222	0.004 (4)	1.3 (4)	//	0.000 (2)
C223	−0.012 (5)	< 2σ	0.000 (< 1)	−0.005(3)
C233	0.018 (5)	< 2σ	//	0.001 (3)
C333	−0.006 (4)	−0.4 (4)	//	0.001 (3)

† This work: multipole model against experimental F_os, with anharmonicity included.   ‡ Artioli *et al.* (1997), neutron diffraction estimates from a *natural* pyrope single crystal. Gram–Charlier coefficients were explicitly refined up to the fourth order.   § '< 2σ' labels Gram–Charlier coefficients that were deemed too low to be reported. Entries marked by '//' were not reported.   ¶ Nakatsuka *et al.* (2011), XRD estimates on a synthetic pyrope sample. No anharmonicity was included on Mg in their final model.   †† Sawada (1993), XRD estimates on a synthetic pyrope sample.

0.0260]. Conversely, in the treatment of Nakatsuka *et al.* (2011), based on 340 data (*versus* our set of 785 observed reflections), the two corresponding agreements were the same.

For sure, there is a general agreement (Pavese *et al.*, 1995, 1998; Nakatsuka *et al.*, 2011, 2013) on the fact that the charge density of Mg is diffused across a somewhat larger volume than Al and Si. On the basis of the aforementioned arguments, one might conclude that Mg disorder, if any, could be *dynamic* in nature. Such a model would indeed account for the highly anisotropic density features around the position 24c and might explain the observed structured Fourier residuals. It is possible that soft phonon modes, together with the significant amount of void space available to Mg, allow instantaneous symmetry breaking of the perfect 24c symmetry. Transient off-site potential energy minima could thus be created, which have a significant probability of being populated. This would result in large vibrations of Mg atoms around their crystallographic positions. As a possible check of this hypothesis, we performed a full vibrational analysis of the pob-TZVP B3LYP normal

modes in the $Ia\bar{3}d$ phase (§2.5 and Table S9). Mg is actually involved in various three-degenerate F low-frequency modes (124–140 cm^{-1}) which imply large (> 0.85 Å) relative stretching displacements with respect to its surrounding O atoms. Large-amplitude bending modes of Mg—O—Mg, Al—O—Mg and Si—O—Mg atom triplets are also present up to 290 cm^{-1}. Accordingly, both hybrid B3LYP and non-hybrid PBE functionals predict the harmonic displacement amplitudes of Mg to be even larger than those of O [U_{eq}(Mg) $\simeq$ 1.3 U_{eq}(O)] at T = 30 K. Interestingly, this is in reasonable agreement with neutron diffraction estimates [U_{eq}(Mg) $\simeq$ 1.1 U_{eq}(O)] (but with anharmonicity included) at the same T.

This provides evidence toward a dynamic, rather than static, coupling mechanism among structure and lattice phonons. However, dynamic disorder implies by itself anharmonic atomic displacements, as the multi-well potential energy surface is, by definition, no longer parabolic in nature (Fig. 6).

Fig. 7 shows the joint probability density functions for the first coordination shells of the three cations in pyrope, while numerical estimates of refined high-order Gram–Charlier terms are given in Table 3, where outcomes from previous studies are also compared. In general, the effect of the anharmonic terms on the atomic p.d.f.'s is rather small (Fig. 7). Some local deviations from perfect ellipsoid shapes are nevertheless appreciable for oxygen and aluminium, whereas the motion of magnesium appears to be dominated by its very large harmonic ADPs.

Inspection of Table S5 shows that 13 out of the 21 correlation coefficients > 0.80 involve parameters of the O atom, with six of them regarding the expected high correlation between coordinates and either dipole coefficients or third-order cumulants. Just five coefficients are higher than 0.9, the largest one (0.94) concerning the correlation between the outer monopoles of Si and Mg. It is well known that high correlation between least-squares parameters increases the corresponding e.s.d.'s. In spite of their large estimated errors, however,
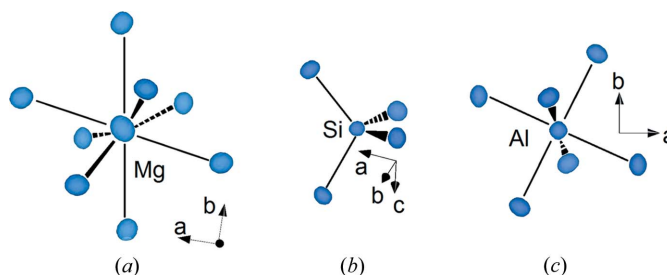

Figure 7
Plot of joint probability density functions for Mg (*a*), Si (*b*) and Al (*c*) in pyrope at T = 30.0 (3) K, as computed through the program *JANA*2006 (Petricek *et al.*, 2014) from the ANH multipole model, which includes anharmonic Gram–Charlier terms. For each picture, the corresponding crystallographic reference system is also given.

Table 4
Properties of the charge density at the (3,−1) BCPs of pyrope.

First row: values of ρ_{EXP}; second row: values of ρ_{MSSF}, third row: values of ρ_{THEO}. Electron density ρ_{BCP} in e Å^{-3}; its Hessian eigenvalues (λ_1, λ_2 and λ_3) and the corresponding Laplacian ($\nabla^2\rho_{BCP}$) in e Å^{-5}; bond ellipticity $\varepsilon = \lambda_1/\lambda_2 - 1$. Distances between atoms and between atoms and BCPs in Å. Energy densities G, V, and H in kJ mol^{-1} per atomic unit volume. Bond degree BD$_{BCP}$ parameter in hartree e^{-1}. Estimated standard deviations in parentheses refer to the last quoted digit.

$X-Y$ interaction	Si—O	Al—O	Mg—O1	Mg—O2	O1—O3	O2—O3
Multiplicity	96	96	96	96	48	48
$X-Y$ distance	1.6354 (3)	1.8848 (3)	2.1960 (4)	2.3326 (4)	2.6980 (5)	2.7690 (5)
X–BCP	0.692	0.798	0.969	1.039	1.349	1.384
	0.693	0.805	0.951	1.002	1.349	1.388
	0.677	0.791	0.932	0.986	1.349	1.384
BCP–Y	0.943	1.086	1.228	1.294	1.349	1.384
	0.944	1.079	1.247	1.330	1.349	1.388
	0.959	1.094	1.265	1.346	1.349	1.384
ρ_{bcp}	0.89 (1)	0.49 (1)	0.27 (1)	0.21 (1)	0.161 (9)	0.147 (7)
	0.809 (3)	0.400 (3)	0.186 (3)	0.141 (3)	0.142 (3)	0.131 (2)
	0.956	0.446	0.200	0.132	0.137	0.114
$\nabla^2\rho_{BCP}$	17.0 (1)	8.26 (8)	3.08 (6)	1.77 (5)	1.69 (2)	1.54 (2)
	19.30 (3)	9.09 (2)	3.944 (9)	2.429 (8)	1.557 (4)	1.439 (4)
	19.287	9.332	4.244	2.701	1.799	1.568
λ_1	−3.96 (7)	−1.61 (4)	−0.72 (2)	−0.46 (2)	−0.291 (4)	−0.158 (5)
	−4.02 (1)	−1.675 (8)	−0.646 (4)	−0.371 (4)	−0.271 (1)	−0.150 (2)
	−6.031	−2.618	−0.943	−0.541	−0.412	−0.293
λ_2	3.90 (7)	−1.61 (4)	−0.61(2)	−0.40 (1)	−0.08 (2)	−0.10 (1)
	−3.96 (1)	−1.666 (8)	−0.543 (4)	−0.325 (3)	−0.225 (3)	−0.150 (1)
	−5.971	−2.577	−0.901	−0.489	−0.296	−0.250
λ_3	24.9 (2)	11.5 (1)	4.41 (6)	2.63 (6)	2.06 (1)	1.80 (1)
	27.28 (3)	12.43 (2)	5.13 (1)	3.13 (1)	2.053 (4)	1.739 (3)
	31.290	14.527	6.088	3.730	2.507	2.111
ε	0.02 (2)	0.00 (3)	0.19 (5)	0.17 (6)	2.5 (8)	0. 6 (2)
	0.014 (5)	0.005 (7)	0.19 (1)	0.14 (2)	0.21 (2)	0.00 (2)
	0.010	0.016	0.047	0.107	0.391	0.170
$G(\mathbf{r})_{BCP}$	566.28	245.25	91.21	55.35	45.59	40.77
	570.17	232.98	90.57	56.05	40.36	36.70
	640.43	250.89	98.46	59.75	44.05	36.86
$V(\mathbf{r})_{BCP}$	−669.57	−265.54	−98.53	−62.49	−45.16	−39.60
	−614.69	−218.39	−73.73	−45.95	−38.32	−34.21
	−755.57	−247.62	−81.33	−45.93	−39.11	−31.00
$H(\mathbf{r})_{BCP}$	−103.28	−20.29	−7.32	−7.14	0.44	1.17
	−44.52	14.59	16.854	10.10	2.04	2.49
	−115.14	3.27	17.13	13.82	4.94	5.85
BD$_{BCP}$	−0.298	−0.106	−0.070	−0.087	0.007	0.020
	−0.141	0.094	0.233	0.184	0.037	0.049
	−0.310	0.019	0.220	0.269	0.093	0.132
$[|V(\mathbf{r})|/G(\mathbf{r})]_{BCP}$	1.18	1.08	1.08	1.13	0.99	0.97
	1.08	0.94	0.81	0.82	0.95	0.93
	1.18	0.99	0.83	0.77	0.89	0.84

several final values of the third- and fourth-order GC coefficients are statistically very significant, being higher than three e.s.d.'s. This is observed for all the three C_{ijk} terms of the Si and Mg atoms, for two D_{iiii} coefficients of Al, for four out of six D_{ijkl} parameters of Mg, and for three of the 10 C_{ijk}s of the O atom (Table 3). Therefore, the overall picture is that of

substantial anharmonic motion affecting all the components of the crystal, but especially the Mg ion.

Previous studies give rather contradictory results or conclusions when they come to the anharmonic contribution to thermal motion (Table 3). The two studies on natural samples (one using neutron diffraction at T = 30 K; Artioli et al., 1997; the other one using X-ray diffraction at room temperature; Sawada, 1993) agree in stating that anharmonicity must be included into the least-squares refinement models, but the numerical values reported for the same GC coefficients differ by orders of magnitude, those at 30 K being much greater than those at 296 K. The anomalous behaviour of several high-order coefficients of the O atom at T = 30 K has been underlined by the authors of the multi-temperature neutron study (Artioli et al., 1997), who noted that '*they are invariably negligible within errors in the room-temperature range, whereas they seem to be non-zero at low temperature*'. On the other hand, differences up to two orders of magnitude are also seen between the neutron results and those from the previous X-ray work (Pavese et al., 1995) at the same 30 K temperature, the latter investigation having confined the modeling of anharmonic dynamical behavior only to the Mg atom (in a synthetic sample). For example, the value of the C_{113} coefficient of this cation was found equal to −1.4 (3) × 10^{-6} from the refinement of the X-ray data, but equal to 2 (2) × 10^{-5} in the neutron case. The corresponding anharmonic term at 296 K was given by Sawada (1993) as −0.6 (4) × 10^{-7}. As stated by Larsen, Stewart and coworkers (Sørensen et al., 2003) a few years ago in a charge-density study of tetra-fluoroterephthalonitrile, where GC coefficients have been derived at the same temperature of 122.4 K from both X-ray and neutron data, '*a proper treatment of anharmonic motion requires data of high resolution and accuracy*'. In view of this statement, it is possible that the neutron results for pyrope suffer from insufficient resolution of the data [(sin θ/λ)$_{max}$ = 0.79 Å^{-1}]. In conclusion, from the current dataset we cannot disentangle possible residual dynamic disorder (associated with a multiple-well form of the potential) from a *pure*

anharmonic motion (where just a non-parabolic minimum is present). What we can say is that we do not see any incontrovertible evidence of static disorder at the Mg position from the current X-ray dataset.

3.4. Topology of $\rho(\mathbf{r})$

3.4.1. Point topological descriptors. Topological descriptors of the charge density and its related scalar fields, as provided by Bader's quantum theory of atoms in molecules (QTAIM; Bader, 1990), grant access to the quantitative analysis of bonding features in solids (Gatti *et al.*, 2016; Saleh *et al.*, 2014; Lo Presti *et al.*, 2014; Saleh *et al.*, 2013; Martins *et al.*, 2016; Macetti *et al.*, 2016; Sovago *et al.*, 2016; Khan *et al.*, 2016; Krawczuk & Macchi, 2014; Hathwar *et al.*, 2011). We have previously documented (Lo Presti *et al.*, 2005; Lo Presti & Destro, 2008), in the case of the transition metal sulfide $FeCr_2S_4$, the usefulness of an exhaustive experimental and theoretical study of the total electron density and its Laplacian. The same approach has been adopted here and applied on experimental, ρ_{EXP}, theoretical multipole-projected, ρ_{MSSF}, and primary theoretical, ρ_{THEO}, electron densities.

In all the three total electron density distributions a total of six unique $(3, -1)$ CPs (critical points), also called bond critical points (BCPs), was found (Table 4), to be compared with the 16 symmetry-independent interatomic separations of Table 1. At each BCP the kinetic $[G(\mathbf{r})_{BCP}]$ and potential $[V(\mathbf{r})_{BCP}]$ contributions to the local energy density $H(\mathbf{r})_{BCP}$, according to

$$H(\mathbf{r})_{BCP} = G(\mathbf{r})_{BCP} + V(\mathbf{r})_{BCP} \qquad (1)$$

were evaluated as functions of $\rho(\mathbf{r})_{BCP}$ and $\nabla^2\rho(\mathbf{r})_{BCP}$, following Abramov (1997) and applying the local form of the virial theorem (Bader, 1990; Espinosa *et al.*, 1998). Furthermore, the bond degree (BD) parameter (Espinosa *et al.*, 2002; Mariam & Musin, 2008), given by the ratio $[H(\mathbf{r})/\rho(\mathbf{r})]_{BCP}$, was calculated for each of the BCPs. All the mentioned properties at these critical points are listed in Table 4, while Fig. 8 shows the $-\nabla^2\rho(\mathbf{r})$ distri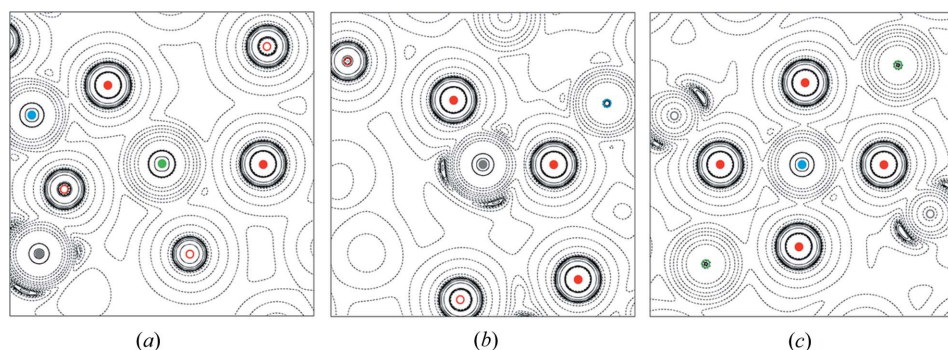bution, as mapped in representative planes around the three cations. Ring (or 3,+1) critical points, RCPs, and cage (or 3,+3) critical points, CCPs, were also located in the three charge-density distributions. They are reported in Tables S7 and S8 of the supporting information, respectively. Inspection of the latter two tables and Table 4 shows that the two multipolar charge densities ρ_{EXP} and ρ_{MSSF} have the same overall topology, while that of ρ_{THEO} displays two significant differences. Indeed, with the same number of RCPs and CCPs (six and two, respectively), the two multipolar charge densities differ only slightly in the location of such CPs, with a maximum separation of 0.37 Å between two corresponding RCPs and of 0.58 Å between the cage CPs observed at *ca* 2 Å from atom Si, the other one being exactly coincident in location.

Taking into account their multiplicities (Table 4), these RCPs and CCPs constitute, together with the BCPs of Table 4, a set of CPs that fully satisfies the Morse invariant relationship (Morse & Cairns, 1969; Jones & March, 1985); thus indicating a self-consistent topology. The primary theoretical density ρ_{THEO} shows instead one more CCP, not found in the experimentally derived models, lying in a plane at $z = 3/8$, and at distances of 1.764 Å from Si and 1.886 Å from O. Furthermore, out of the six RCPs found in this ρ, one is observed where no corresponding CP appears in the multipolar charge density distributions, at 1.808 Å from Mg, while the RCP observed at $z = 3/8$ in both multipolar ρs is here missing, or, better, corresponds to the third CCP of ρ_{THEO}. The distance between these two points (*i.e.* the latter, third CCP of the primary density and the RCP of ρ_{EXP}) amounts to 0.279 Å. Inspection of the curvatures λs of the two CPs suggests that λ_1 of ρ_{EXP}, close to zero and negative, has changed into a small but positive curvature in ρ_{THEO}, and the change of sign converts the RCP into a CCP. In spite of these differences, ρ_{THEO} is also topologically self-consistent, thanks to the specific multiplicity of the two different critical points.

The features of the $\nabla^2\rho(\mathbf{r})$ distribution shown in Fig. 8 mirror the point topological descriptors reported in Table 4, but provide at the same time deeper insights into the analogies and differences of the coordination geometries of various cations. In general, the latter have valence shells dominated by charge depletion regions (CDRs). This is expected in a crystal dominated by ionic bonds (Lo Presti & Destro, 2008), where charge transfer is conspicuous and ions bear charges close to their formal oxidation state (see also §3.4.2 below). The cations indeed tend to lose their outermost electrons, so the BCP is located in the CDR of the anion, where $\rho(\mathbf{r})$ is rather flat and its Laplacian possibly close to zero. From Fig. 8 it is evident that the CDR around Si (Fig. 8*b*) is significantly more

Figure 8
Experimentally derived contour maps of $-\nabla^2\rho(\mathbf{r})$ in representative planes (7×7 Å) around cations in pyrope at $T = 30$ K. Contours are plotted at variable intervals in units of e Å^{-5}. Solid lines show the negative regions of the Laplacian (indicating charge concentration), dashed lines the positive regions (indicating charge depletion). Full (open) circles (red: O; green: Mg; blue: Al; grey: Si) mark positions of atoms lying within (more distant than) ± 0.1 Å from the plane of the drawing. (*a*) Plane through Mg (x, y, z), O $(-x, y, -\frac{1}{2} + z)$ and O $(-y, 1 - z, -x)$; (*b*) view along the body diagonal [111] in the (111) plane passing through Si $(-\frac{1}{4} + y, \frac{1}{4} + x, \frac{1}{4} - z)$, O $(y, -\frac{1}{2} + z, -x)$ and O $(\frac{3}{4} - z, \frac{1}{4} + y, -\frac{1}{4} + x)$; (*c*) plane through Al $(\frac{1}{4} + y, \frac{1}{4} - x, -\frac{1}{4} + z)$, O $(\frac{1}{4} - y, \frac{1}{4} - x, \frac{1}{4} - z)$ and O $(\frac{3}{4} - z, \frac{1}{4} + y, -\frac{1}{4} + x)$.

research papers

Table 5
Integrated volume of atomic basin (V_Ω), integrated atomic charge (ρ_Ω) and net charge (Q) for the four atomic species of pyrope.

Integration of the multipole charge densities ρ_{EXP} and ρ_{MSSF} performed through the *VALRAY* code (Stewart *et al.*, 2000), where a conservative estimate of the uncertainty in the integrated properties is *ca* 5%. Integration of ρ_{THEO} performed by *CRYSTAL*14 (Dovesi *et al.*, 2014).

Atom	V_Ω (Å^3)			ρ_Ω (e)			Q (e)		
	EXP	MSSF	THEO	EXP	MSSF	THEO	EXP	MSSF	THEO
Si	5.74	5.24	3.184	11.18	11.26	10.812	+2.82	+2.74	+3.188
Al	4.16	3.73	3.205	10.31	10.46	10.429	+2.69	+2.54	+2.571
Mg	6.98	5.29	5.031	10.38	10.19	10.222	+1.62	+1.81	+1.778
O	11.72	12.34	13.013	9.55	9.56	9.670	−1.55	−1.56	−1.670
$\sum V_\Omega$†	1496.96	1497.04	1497.688						
$\sum \rho_\Omega$‡				1599.20	1599.92	1600.00			
$\sum Q$§							+0.10	+0.01	0.000

† Sum of the atomic volumes in the cell, to be compared with the unit-cell volume, 1497.4 Å^3.   ‡ Sum of the atomic charges in the cell, to be compared with the total number of electrons in the cell, $F(000) = 1600\ e$.   § Sum of the net atomic charges in the pyrope formula unit (Mg$_3$Al$_2$Si$_3$O$_{12}$), which should be formally zero.

structured than those of Mg and Al [Figs. 8(*a*) and 8(*c*)], which are almost spherically symmetric. More in detail, deep localized CDRs appear close to Si, in zones relatively far from direct Si—O bonds [see Si atoms in Figs. 8(*a*), 8(*b*) and 8(*c*)]. These anisotropies in the $\nabla^2\rho(\mathbf{r})$ distribution can be ascribed to the fact that the bond regions of Si, though dominated by charge depletion features, are anyway prone to attract charge from other zones of the valence shell. In other words, despite their evident ionic nature, Si—O interactions show a higher degree of covalency than Mg—O and Al—O interactions. This is in good agreement with the value of $\nabla^2\rho_{BCP}$ at the Si—O critical point (Table 4), which is $\sim$ 2–4 times larger than those at the Mg—O and Al—O ones, being also associated with a negative BD parameter (Table 4) We note also that Si has the lowest positive charge with respect to its formal oxidation state ($\sim$ +2.9 *versus* +4; see §3.4.2).

A detailed comparison among the properties of the three charge densities can be found in the supporting information (§S7), where our topological quantities of pyrope are also compared with those reported by Gibbs *et al.* (2008) in their review on bonded interactions and the crystal chemistry of minerals. We can safely conclude that $\rho_{EXP}(\mathbf{r})$ is fully consistent with the theoretical one, at least once the multipole model bias is taken into account (Lo Presti & Gatti, 2009).

3.4.2. Atomic volumes and charges. In Bader's QTAIM an atom in a material is defined by its nucleus plus an appropriate portion of the total electron density, enclosed by a zero flux surface of $\nabla\rho(\mathbf{r})$, which defines an atomic basin Ω. Several properties can then be determined by integration over such a region. Two quantities of particular interest for each atom of pyrope are the atomic volume V_Ω and the number of electrons in the basin (Bosenick & Geiger, 1997; Flensburg & Madsen, 2000), and hence the electronic charge associated with them (Table 5). Net charges were obtained by adding the nuclear charge of each atom to the integrated atomic ρ_Ωs. It is seen that the summations of the atomic volumes for the unit cell give values that are within $\pm$ 0.03% with respect to the value of the experimental unit-cell volume. The corresponding summations of the electron populations give $F(000)$ (*i.e.* the

total number of electrons in the unit cell) with a largest deviation (in ρ_{EXP}) of only 0.05%. These figures prove the reliability of the integration procedure. The values of the atomic ρ_Ωs from the two multipolar charge densities are in excellent agreement, the largest difference not exceeding 1.8% (at the Mg atom), to be compared with an asserted (Flensburg & Madsen, 2000) estimated uncertainty for each integrated quantity of *ca* 5%. This occurs in spite of a much larger difference between the atomic volumes V_Ω for the Mg cation in the two ρs, the value in $V_{\Omega EXP}$ being larger than that in $V_{\Omega MSSF}$ by *ca* 24%. The largest difference between theoretical and experimental values for the atomic electron population is seen at the Si atom, where ρ_Ω is smaller in ρ_{THEO} than in ρ_{EXP} by 3.3%, and the difference is even larger (*ca* 4%) if the value in the primary density is compared with that in ρ_{MSSF}.

All the four atomic volume (V_Ω) values of ρ_{MSSF} are intermediate between those of the other two electron density distributions, with the V_Ω value of the Mg cation closer to the value in ρ_{THEO} ($\Delta \simeq$ 5%) than to that in ρ_{EXP} ($\Delta \simeq$ 24%). Conversely, those of the Si, Al and O atoms are closer to the values in ρ_{EXP} (with $\Delta \simeq$ 9, 10 and 5%, respectively) than to the estimates in the primary density ($\Delta \simeq$ 39, 14 and 5%, respectively). As already noted for the electron populations, the largest difference between theoretical and experimental V_Ω values is shown by the Si atom, where the theoretical value is *ca* 44% smaller than that in the experimental multipolar electron density. Differences for the other three atoms are anyhow also very large: 23% and 28% for Al and Mg, respectively, and 10% for O. Differences in V_Ω between theoretical and experimental charge density distributions are quite common (Lo Presti *et al.*, 2008; Saleh *et al.*, 2013), as the atomic boundaries critically depend on the gradient field in the internuclear regions, which in ionic compounds are characterized by very low $\rho(\mathbf{r})$ and are therefore sensitive to very fine details of the least-squares and quantum models. On the other hand, when the charge density is integrated over each atomic basin, excellent agreement is found between theoretical and experimental $\rho(\mathbf{r})$ distributions. This means that our

Acta Cryst. (2017). B**73**, 722–736   Riccardo Destro *et al.* · Anharmonic motions *versus* dynamic disorder   **733**

model for the charge density is fully consistent with atomic populations derived quantum mechanically for an ideal, infinite crystal without any kind of disorder.

4. Conclusions

Both recently and in the past, contrasting interpretations (static disorder/anharmonic atomic displacements) have been proposed to explain structured residual charge density features close to the Mg 24c lattice site in the pyrope garnet. The problem has no obvious solutions as, on the one hand, static disorder and anharmonicity produce very similar effects in $\Delta\rho$ maps and, on the other hand, somewhat incomplete (X-ray) or low-resolution (neutron) diffraction data sets were employed until now. In this work, we provide very accurate and precise data, consisting of the whole set of 788 independent reflections out to a maximum resolution of 0.44 Å, collected at $T = 30.0$ (3) K. At variance with previous works, neither intense low-order reflections nor weak high-order data were discarded, and all the possible sources of systematic errors were properly accounted for and corrected. Various multipole electron density models were compared, including either anharmonic terms on all the ions or various displacive disorder models at the Mg site. Even though the volume of the reciprocal space explored is still too low to fulfill Kuhs' condition for a totally unbiased refinement of Gram–Charlier coefficients, we are confident that the quality of our dataset is high enough to detect, if present, any significant effects affecting low-order diffraction intensities, which in turn might depend on both disorder and anharmonicity. The only relevant structured features we have detected in the Fourier maps are two very low ($\simeq 0.1$–0.15 e Å^{-3}) positive peaks 0.58 Å away from Mg, along the [001] axis. Any attempt to explicitly include this displacement into the multipole model invariably resulted in the ion brought back to its original, undisplaced 24c position within a few (< 2) thousandths of Å. The 96 h displacive model proposed by Nakatsuka et al. (2011) is also incompatible with our dataset, resulting in a worse F_o–F_c agreement in conjunction with a small ion displacement (0.06 Å), falling within the harmonic thermal ellipsoid envelope at a 50% probability level.

A full vibrational analysis of the pob-TZVP B3LYP normal modes in the $Ia\bar{3}d$ phase has shown that Mg is involved in several soft phonon modes, which imply large (> 0.85 Å) relative stretching and bending displacements with respect to its surrounding O atoms. In agreement with neutron estimates, the harmonic displacement amplitudes of this ion are predicted to be even larger than those of O [$U_{eq}(Mg) \simeq 1.3$ $U_{eq}(O)$] at $T = 30$ K.

Our study conforms to the general agreement (Pavese et al., 1995, 1998; Nakatsuka et al., 2011, 2013) on the fact that the charge density of Mg is diffused across a somewhat larger volume than Al and Si. Invoking the presence of some kind of dynamic disorder might reconcile the intertwined views of anharmonicity and disorder. Such a model would indeed account for the highly anisotropic density features around the position 24c reported in this and previous works, and might explain the observed structured Fourier residuals very close to the Mg ion. It is possible that soft phonon modes, together with the significant amount of void space available to Mg, allow instantaneous symmetry breaking of the perfect 24c symmetry. Transient off-site potential energy minima could thus be created, which have a significant probability of being populated. Mg^{2+} ions essentially 'rattle' in a very large cavity, resulting in large vibrations and, consequently, also in nonnegligible anharmonic contributions to thermal motion even at very low T. Actually, dynamic disorder implies by itself anharmonic atomic displacements, as the multi-well potential energy surface is, by definition, no longer parabolic in nature. For this reason, we believe that additional experiments are required to definitely solve the issue, in particular X-ray diffraction experiments, to be carried out at very high resolution, possibly up to $(\sin\theta/\lambda)_{max} = 1.8$–$2.0$ Å, by means of low-wavelength synchrotron radiation. At the same time, inelastic scattering measurements, mapping the phonon dispersion curves at low T, would be extremely useful to detect any further deviation from the purely harmonic behaviour. Such experiments will help in disclosing whether the potential energy surface bears two minima close to the Mg 24c site or not. In the first case, our hypothesis of occurring dynamic disorder would be fulfilled.

On the other hand, we expect that *static* disorder should be entangled with some kind of stronger anisotropy in the crystal field, as the existence of two or more well defined minima, separated by intersite barriers high enough to hamper Mg exchange among populated off-lattice sites even at $T \gg 30$ K, would imply a much larger distortion. However, we do not see any evidence for that. Rather, residual Fourier maps, integrated atomic charges, very good agreement between an ideal $\rho(\mathbf{r})$ model for a perfectly ordered crystal with the XRD-derived charge density all imply that there is no incontrovertible evidence of static disorder at the Mg position.

5. Related literature

References cited in the supporting information include: Becke (1993), Becker & Coppens (1974), Clementi & Roetti (1974), and Lee et al. (1988).

References

Abramov, Yu. A. (1997). Acta Cryst. A**53**, 264–272.

Andrés, J., Beltrán, A. & Igualada, J. A. (1995). *J. Phys. Chem. Solids*, **56**, 901–906.

Armbruster, T., Geiger, C. A. & Lager, G. A. (1992). *Am. Mineral.* **77**, 512–521.

Artioli, G., Pavese, A., Ståhl, K. & McMullan, R. K. (1997). *Can. Mineral.* **35**, 1009–1019.

Bader, R. F. W. (1990). *Atoms in Molecules: a Quantum Theory.* Oxford University Press.

Becke, A. D. (1993). *J. Chem. Phys.* **98**, 5648–5652.

Becker, P. J. & Coppens, P. (1974). *Acta Cryst.* A**30**, 129–147.

Bosenick, A. & Geiger, C. A. (1997). *J. Geophys. Res.* **102**, 22649–22657.

Brünger, A. T. (1992). *Nature*, **355**, 472–475.

Buschmann, H., Berendts, S., Mogwitz, B. & Janek, J. (2012). *J. Power Sources*, **206**, 236–244.

Christensen, M., Johnsen, M. & Iversen, B. B. (2010). *Dalton Trans.* **39**, 978–992.

Christensen, S., Avila, M.A., Suekuni, K., Piltz, R., Takabatake, T. & Christensen, M. (2013). *Dalton Trans.* **42**, 14766–14775.

Clementi, E. & Roetti, C. (1974). *Atom. Data Nucl. Data*, **14**, 177–478.

Cruickshank, D. W. J. (1949). *Acta Cryst.* **2**, 65–82.

Crystal Impact (2014). *DIAMOND*. Crystal Impact GbR, Bonn, Germany.

D'Arco, P., Fava, F. F., Dovesi, R. & Saunders, V. R. (1996). *J. Phys. Condens. Matter*, **8**, 8815–8828.

Destro, R. (1988). *Aust. J. Phys.* **41**, 503–510.

Destro, R., Loconte, L., Lo Presti, L., Roversi, P. & Soave, R. (2004). *Acta Cryst.* A**60**, 365–370.

Destro, R., Lo Presti, L., Soave, R. & Goetha, A. E. (2010). *Modern Charge Density Analysis*, edited by C. Gatti and P. Macchi. Berlin: Springer.

Destro, R. & Marsh, R. E. (1987). *Acta Cryst.* A**43**, 711–718.

Destro, R. & Marsh, R. E. (1993). *Acta Cryst.* A**49**, 183–190.

Destro, R., Roversi, P., Barzaghi, M. & Marsh, R. E. (2000). *J. Phys. Chem. A*, **104**, 1047–1054.

Destro, R., Soave, R., Barzaghi, M. & Lo Presti, L. (2005). *Chem. Eur. J.* **11**, 4621–4634.

Dove, M. T. (1997). *Am. Mineral.* **82**, 213–244.

Dovesi, R., De La Pierre, M., Ferrari, A. M., Pascale, F., Maschio, L. & Zicovich-Wilson, C. M. (2011). *Am. Mineral.* **96**, 1787–1798.

Dovesi, R., Saunders, V. R., Roetti, C., Orlando, R., Zicovich-Wilson, C. M., Pascale, F., Civalleri, B., Doll, K., Harrison, N. M., Bush, I. J., D'Arco, P. & Llunell, M. (2014). *CRYSTAL User's Manual.* University of Torino, Italy.

Erba, A., Ferrabone, A., Orlando, R. & Dovesi, R. (2013). *J. Comput. Chem.* **34**, 346–354.

Erba, A., Mahmoud, A., Belmonte, D. & Dovesi, R. (2014*a*). *J. Chem. Phys.* **140**, 124703.

Erba, A., Mahmoud, A., Orlando, R. & Dovesi, R. (2014*b*). *Phys. Chem. Miner.* **41**, 151–160.

Espinosa, E., Alkorta, I., Elguero, J. & Molins, E. (2002). *J. Chem. Phys.* **117**, 5529–5542.

Espinosa, E., Molins, E. & Lecomte, C. (1998). *Chem. Phys. Lett.* **285**, 170–173.

Flensburg, C. & Madsen, D. (2000). *Acta Cryst.* A**56**, 24–28.

Galven, C., Fourquet, J. L., Crosnier-Lopez, M. P. & Le Berre, F. (2011). *Chem. Mater.* **23**, 1892–1900.

Gatti, C., Saleh, G. & Lo Presti, L. (2016). *Acta Cryst.* B**72**, 180–193.

Geiger, C. A. (2013*a*). *Elements*, **9**, 447–452.

Geiger, C. A. (2013*b*). *Am. Mineral.* **98**, 780–782.

Gibbs, G. V., Downs, R. T., Cox, D. F., Ross, N. L., Prewitt, C. T., Rosso, K. M., Lippmann, T. & Kirfel, A. (2008). *Z. Kristallogr.* **223**, 1–40.

Hamilton, W. C. (1965). *Acta Cryst.* **18**, 502–510.

Haselton, H. T. & Westrum, E. F. Jr (1980). *Geochim. Cosmochim. Acta*, **44**, 701–709.

Hathwar, V. R. T., Thakur, T. S., Dubey, R., Pavan, M. S., Guru Row, T. N. & Desiraju, G. R. (2011). *J. Phys. Chem. A*, **115**, 12852–12863.

Herbst-Irmer, R., Henn, J., Holstein, J. L., Hübschle, C. B., Dittrich, B., Stern, D., Kratzert, D. & Stalke, D. (2013). *J. Phys. Chem. A*, **117**, 633–641.

Huang, S. (2014). FIU Electronic Theses and Dissertations. Paper 1185 (http://digitalcommons.fiu.edu/etd/1185).

Jones, W. & March, N. H. (1985). *Theoretical Solid State Physics*, Vol. 1. New York: Dover.

Jørgensen, M. R. V., Hathwar, V. R., Bindzus, N., Wahlberg, N., Chen, Y.-S., Overgaard, J. & Iversen, B. B. (2014). *IUCrJ*, **1**, 267–280.

Kastbjerg, S., Bindzus, N., Søndergaard, M., Johnsen, S., Lock, N., Christensen, M., Takata, M., Spackman, M. A. & Brummerstedt Iversen, B. (2013). *Adv. Funct. Mater.* **23**, 5477–5483.

Kawai, K. & Tsuchiya, T. (2015). *Phys. Earth Planet. Inter.* **240**, 125–131.

Khan, I., Panini, P., Khan, S. U.-D., Rana, U. A., Andleeb, H., Chopra, D., Hameed, S. & Simpson, J. (2016). *Cryst. Growth Des.* **16**, 1371–1386.

Kisi, E. & Yuxiang, M. (1998). *J. Phys. Condens. Matter*, **10**, 3823–3832.

Krawczuk, A. & Macchi, P. (2014). *Chem. Cent. J.* **8**, 68.

Kuhs, W. F. (1988). *Aust. J. Phys.* **41**, 369–382.

Kuhs, W. F. (1992). *Acta Cryst.* A**48**, 80–98.

Lee, C., Yang, W. & Parr, R. G. (1988). *Phys. Rev. B*, **37**, 785–789.

Li, L., Long, H., Raterron, P. & Weidner, D. (2006). *Am. Mineral.* **91**, 517–525.

Li, L., Weidner, D. J., Brodholt, J., Alfè, D. & Price, G. D. (2011). *J. Earth Sci. China*, **22**, 169–175.

Lo Presti, L. & Destro, R. (2008). *J. Chem. Phys.* **128**, 044710.

Lo Presti, L. & Gatti, C. (2009). *Chem. Phys. Lett.* **476**, 308–316.

Lo Presti, L., Invernizzi, D., Soave, R. & Destro, R. (2005). *Chem. Phys. Lett.* **416**, 28–32.

Lo Presti, L., Sist, M., Loconte, L., Pinto, A., Tamborini, L. & Gatti, C. (2014). *Cryst. Growth Des.* **14**, 5822–5833.

Lo Presti, L., Soave, R. & Destro, R. (2006). *J. Phys. Chem. B*, **110**, 6405–6414.

Macetti, G., Loconte, L., Rizzato, S., Gatti, C. & Lo Presti, L. (2016). *Cryst. Growth Des.* **16**, 6043–6054.

Mariam, Y. H. & Musin, R. N. (2008). *J. Phys. Chem. A*, **112**, 134–145.

Martins, M. A. P., Hörner, M., Beck, J., Tier, A. Z., Belladona, A. L., Meyer, A. R., Zanatta, N., Bonacorso, H. G. & Frizzo, C. P. (2016). *CrystEngComm*, **18**, 3866–3876.

Maschio, L., Kirtman, B., Salustro, S., Zicovich-Wilson, C. M., Orlando, R. & Dovesi, R. (2013). *J. Phys. Chem. A*, **117**, 11464–11471.

Massaro, F. R., Bruno, M. & Nestola, F. (2014). *Cryst. Growth Des.* **14**, 2357–2365.

Milani, S., Nestola, F., Alvaro, M., Pasqual, D., Mazzucchelli, M. L., Domeneghetti, M. C. & Geiger, C. A. (2015). *Lithos*, **227**, 140–147.

Mondal, S., Bykova, E., Dey, S., Ali, S. I., Dubrovinskaia, N., Dubrovinsky, L., Parakhonskiy, G. & van Smaalen, S. (2016). *Sci. Rep.* **6**, 19330.

Morse, M. & Cairns, S. S. (1969). *Critical Point Theory in Global Analysis and Differential Geometry.* New York: Academic Press.

Nakatsuka, A., Shimokawa, M., Nakayama, N., Ohtaka, O., Arima, H., Okube, M. & Yoshiasa, A. (2011). *Am. Mineral.* **96**, 1593–1605.

Nakatsuka, A., Shimokawa, M., Nakayama, N., Ohtaka, O., Arima, H., Okube, M. & Yoshiasa, A. (2013). *Am. Mineral.* **98**, 783–784.

Nishimura, S., Suzuki, Y., Lu, J., Torii, S., Kamiyama, T. & Yamada, A. (2016). *Chem. Mater.* **28**, 2393–2399.

Palke, A. C., Stebbins, J. F., Geiger, C. A. & Tippelt, G. (2015). *Am. Mineral.* **100**, 536–547.

Pavese, A., Artioli, G. & Moze, O. (1998). *Eur. J. Mineral.* **10**, 59–70.

Pavese, A., Artioli, G. & Prencipe, M. (1995). *Am. Mineral.* **80**, 457–464.

Peintinger, M. F., Oliveira, D. V. & Bredow, T. (2013). *J. Comput. Chem.* **34**, 451–459.

Petricek, V., Dusek, M. & Palatinus, L. (2014). *Z. Kristallogr.* **229**, 345–352.

Pilati, T., Demartin, F. & Gramaccioli, C. M. (1996). *Acta Cryst.* B**52**, 239–250.

Pinzaru, D. & Thangadurai, V. (2014). *J. Electrochem. Soc.* **161**, A2060–A2067.

Renninger, M. (1937). *Z. Phys.* **106**, 141–176.

Saleh, G., Gatti, C. & Lo Presti, L. (2014). *Comput. Theor. Chem.* **1053**, 53–59.

Saleh, G., Soave, R., Lo Presti, L. & Destro, R. (2013). *Chem. Eur. J.* **19**, 3490–3503.

Samson, S., Goldish, E. & Dick, C. J. (1980). *J. Appl. Cryst.* **13**, 425–432.

Sawada, H. (1993). *Z. Kristallogr.* **203**, 41–48.

Scheins, S., Zheng, S.-L., Benedict, J. B. & Coppens, P. (2010). *Acta Cryst.* B**66**, 366–372.

Schmidt, W., Bottke, P., Sternad, M., Gollob, P., Hennige, V. & Wilkening, M. (2015). *Chem. Mater.* **27**, 1740–1750.

Sørensen, H. O., Stewart, R. F., McIntyre, G. J. & Larsen, S. (2003). *Acta Cryst.* A**59**, 540–550.

Sovago, I., Gutmann, M. J., Senn, H. M., Thomas, L. H., Wilson, C. C. & Farrugia, L. J. (2016). *Acta Cryst.* B**72**, 39–50.

Stash, A. (2007). *DRKplot* for *XD* and *SHELXL*. Moscow, Russian Federation.

Stewart, R. F. (1976). *Acta Cryst.* A**32**, 565–574.

Stewart, R. F. (1980). *Electron and Magnetization Densities in Molecules and Solids*, edited by P. Becker, pp. 427–431. New York: Plenum Press.

Stewart, R. F., Spackman, M. A. & Flensburg, C. (2000). *VALRAY User's Manual, Version 2.1.* Carnegie Mellon University Press, Pittsburgh, USA, and University of Copenhagen Press, Copenhagen, Denmark.

Thangadurai, V., Pinzaru, D., Narayanan, S. & Baral, A. K. (2015). *J. Phys. Chem. Lett.* **6**, 292–299.

Thornley, F. R., Kennedy, N. S. J. & Nelmes, R. J. (1976). *J. Phys. C Solid State Phys.* **9**, 681–692.

Zhong, J., Zhuang, W., Xing, X., Liu, R., Li, Y., Liu, Y. & Hu, Y. (2015). *J. Phys. Chem. C*, **119**, 5562–5569.